



# Carbon nanofibers embedded with Fe–Co alloy nanoparticles via electrospinning as lightweight high-performance electromagnetic wave absorbers

Wen-Jun Cai, Jian-Guo Jiang, Zi-Dong Zhang\* , Zi-Xuan Liu, Lu-Jie Zhang, Zhen-Kun Long, Ke Bi

Received: 19 July 2023 / Revised: 16 August 2023 / Accepted: 20 August 2023 / Published online: 29 February 2024  
© Youke Publishing Co., Ltd. 2024

**Abstract** As a lot of electromagnetic pollution and interference issues have emerged, to overcome electromagnetic interference, prevent electromagnetic hazards, and develop new high-performance electromagnetic wave (EMW) absorbers have become a significant task in the field of materials science. In this paper, a three-dimensional (3D) carbon nanofibers network with core–shell structure, embedded with varied molar ratios of iron and cobalt (4:0, 3:1, 2:2, 1:3, 0:4), was effectively synthesized (Fe/Co@C-CNFs) via electrospinning. The phase, microstructure, magnetic and EMW absorption properties were studied. It is discovered that Fe/Co@C-CNFs doped with iron:cobalt = 1:1 have excellent EMW absorption capacity. When the matching thickness is 1.08 mm, the minimum reflection loss (RL) value is  $-18.66$  dB, while the maximum effective absorption bandwidth (EAB) reaches

4.2 GHz (13.9–18 GHz) at a thickness of 1.22 mm. This is owing to the absorbers' superior impedance matching and multiple reflections as well as the conductivity, dielectric, and magnetic losses of carbon nanofibers embedded with Fe–Co alloy particles. In addition, the radar cross section (RCS) of the absorbers has been calculated by CST Studio Suite, showing that the absorbing coating can effectively reduce the RCS at various angles, especially for Fe/Co@C-CNFs doped with iron:cobalt = 1:1. These findings not only provide new insights for the preparation of lightweight and high-performance electromagnetic wave absorbers, but also contribute to energy storage and conversion.

**Keywords** Electromagnetic wave (EMW) absorbers; Fe/Co@C-CNFs; Core–shell structure; EMW absorbing mechanism; Radar cross section (RCS)

**Supplementary Information** The online version contains supplementary material available at <https://doi.org/10.1007/s12598-023-02592-7>.

W.-J. Cai, Z.-D. Zhang\*, Z.-X. Liu, L.-J. Zhang, Z.-K. Long  
Key Laboratory for Liquid-Solid Structural Evolution and Processing of Materials (Ministry of Education), Shandong University, Jinan 250061, China  
e-mail: zhangzidong@sdu.edu.cn

W.-J. Cai, Z.-D. Zhang, Z.-X. Liu, L.-J. Zhang, Z.-K. Long  
School of Materials Science and Engineering, Shandong University, Jinan 250061, China

J.-G. Jiang  
Energy Institute, Qilu University of Technology (Shandong Academy of Sciences), Jinan 250014, China

K. Bi  
State Key Laboratory of Information Photonics and Optical Communications, School of Science, Beijing University of Posts and Telecommunications, Beijing 100876, China

## 1 Introduction

With the increasingly vigorous development of the information technology industry, modern communication technology is developing in the direction of high density, high integration and wide area coverage [1]. The proliferation of wireless access stations complicates the electromagnetic environment and causes severe active/passive electromagnetic interference issues for electronic devices [2]. It will not only adversely affect the normal use of information terminals, but also cause information leakage and pose security risks [3–6]. Meanwhile, in the field of energy storage and conversion, electromagnetic wave (EMW) absorption materials play a significant role in the exploration of advanced solar energy devices and other related applications [7].



In general, the preparation of absorbing materials should take into account both impedance matching characteristics and attenuation properties of the materials [8]. More EMW can enter the absorbers with good impedance matching, and can be absorbed in materials with high attenuation. In recent years, with the in-depth research of absorbing materials, scholars have preferred to pursue strong absorption, light weight, thin thickness and wideband EMW absorbers [9–12]. The benefits of carbon materials, such as their vast surface area, low density, superior conductivity, stable chemical and physical properties, and cost-effective manufacturing cost, have led to their widespread application in EMW absorbers [13–15]. However, carbon materials also have some shortcomings, such as single loss mechanism and poor multi-band absorption performance, high conductivity resulting in serious skin effect and impedance matching imbalance, narrow absorption band leading to limited application, etc. [16–18]. In previous reports, scholars have improved carbon materials by designing and adjusting the microstructure and morphology of carbon materials and compounding carbon with other functional materials. Numerous researches have demonstrated that the addition of magnetic nanoparticles (Fe, Co, etc.) can improve the EMW attenuation ability of carbon materials [19–22]. For example, Wang et al. [23] prepared Fe/C porous nanofibers (FeCPNFs) by electrospinning, which had three dimensional (3D) cross-linked network structure with low graphitization degree. The minimum reflection loss (RL) of FeCPNFs could reach  $-56.6$  dB at matching frequency (4.96 GHz) and matching thickness (4.29 mm). And the effective absorption bandwidth (EAB) was 3.00 GHz with a thickness of 2.00 mm. Liu et al. [24] synthesized Fe@Fe<sub>3</sub>C/porous carbon, whose RL<sub>min</sub> reached  $-56.88$  dB at 11.3 GHz with a thickness of 2.11 mm, and EAB could get up to 5.2 GHz (from 12.9 to 18 GHz) with a thickness of 1.64 mm. However, to the best of our knowledge, the absorber is usually achieved with a thickness of more than 2 mm in order to achieve a wider EAB; that is to say, there have been few studies on overcoming the extremely thin and light absorbers so far.

In this study, a sequence of carbon nanofibers embedded with Fe–Co alloy nanoparticles were synthesized via electrospinning, resulting in vary absorption capabilities. The effects of varied Fe/Co ratios on the microstructure, electromagnetic parameters, and absorbing properties were investigated. When the molar ratio of Fe and Co was 1:1, the obtained Fe/Co@C-CNFs had the best absorbing property: the EAB of the nanocomposite fibers reached 4.2 GHz at a thickness of 1.22 mm, and the minimum RL reached  $-18.66$  dB at a thickness of 1.08 mm. In addition, the RCS value of the material coating was calculated by CST Studio Suite (CST), which verified that the

absorbing coating could effectively reduce the RCS at various angles in practical application.

## 2 Experimental

Fe/Co@C-CNFs were prepared by electrospinning the solutions with varied ratios of iron and cobalt salt concentrations and subsequent heat treatment, as shown in Fig. 1. First, 1.0 g of polyacrylonitrile (PAN) was dissolved in 9.0 g of N, N-dimethylformamide (DMF) and stirred at 40 °C to fully dissolve. The aforementioned solution was then supplemented with iron and cobalt acetylacetonates, making sure that the combined molar concentration of the two salts was 0.003 mol. The mixture was stirred at 40 °C to form a uniform precursor solution. Then, it was drawn using a 20 ml syringe for electrospinning. The electrospinning parameters were as follows: 15 cm collecting distance, 0.04 mm·min<sup>-1</sup> feeding rate, and 16 kV voltage between the needle's lip and the aluminum foil. After the end of electrospinning, the samples were put into a drying oven at 60 °C for 12 h and pre-oxidized at 240 °C for 2 h. Finally, the pre-oxidized samples were carbonized under a nitrogen atmosphere (carbonization conditions were maintained for 2 h at 800 °C) to obtain carbon nanofibers embedded with magnetic nanoparticles. Under the same molar of total metal salts, the molar ratios of iron and cobalt were adjusted from 4:0, 3:1, 2:2, 1:3 to 0:4, and the corresponding Fe/Co@C-CNFs products were marked as F4N0, F3N1, F2N2, F1N3 and F0C4, respectively.

Phase analysis of the as-synthesized products was performed by powder X-ray diffraction (XRD) on a D/max rB-2500PC diffractometer at a voltage of 45 kV and a current of 50.0 mA with graphite monochromatized Cu K $\alpha$  ( $\lambda = 0.154056$  nm) radiation. Raman spectra of Fe/Co@C-CNFs were recorded on a Raman spectrum (Renishaw in Via) with a 532 nm laser. The micro-morphology was analyzed by field-emission scanning electron microscopy (SEM, SU-70) and high-resolution transmission electron microscopy (HRTEM, FEI Tecnai F20). The hysteresis loops of Fe/Co@C-CNFs at room temperature were measured by a vibrating sample magnetometer (VSM, Lake Shore, 7404). To prepare a composite material for EMW measurement, Fe/Co@C-CNFs were uniformly dispersed in the paraffin matrix with a filler content of 15 wt%. Then the powder was pressed into a ring with an outer diameter of 7.00 mm and an inner diameter of 3.04 mm. The vector network analyzer (VNA, Agilent, E5071C) detected complex permittivity ( $\epsilon_r = \epsilon' - j\epsilon''$ ) and complex permeability ( $\mu_r = \mu' - j\mu''$ ) in the range of 2–18 GHz using the transmission/reflection coaxial line method.

Radar cross section (RCS) is a physical quantity of the echo intensity generated by the target under the irradiation

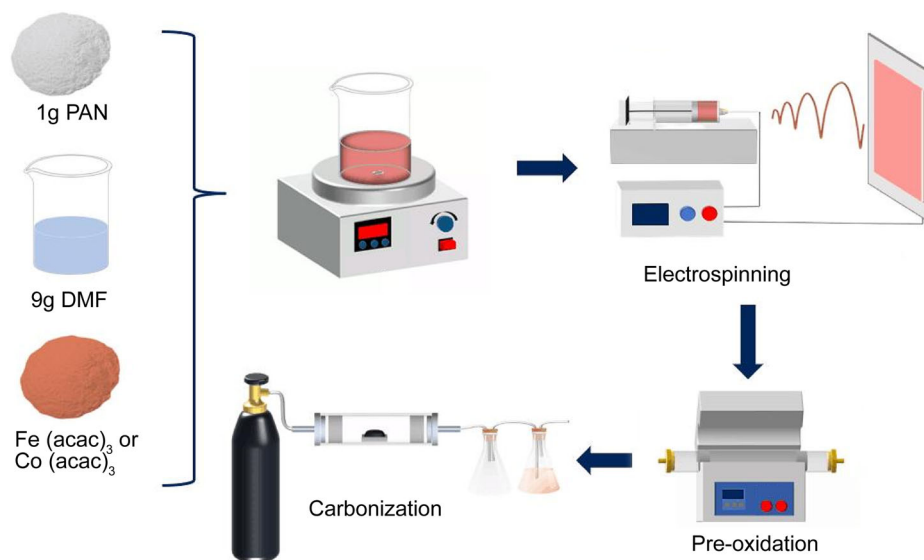


**Fig. 1** Schematic diagram of fabrication process of Fe/Co@C-CNFs

of EMW. In order to simulate the application of Fe/Co@C-CNFs in the real scene, CST was used to build a model of the absorbing coating (thickness = 1.22 mm) with a bottom perfect electrical conductor (PEC) substrate (thickness = 1 mm). The model was 200 mm by 200 mm in size and was placed in the *XY* plane. The field monitor frequency was set at 15 GHz (the middle frequency of Ku band). The RCS values ( $\sigma$ , dB·m<sup>2</sup>) were calculated by Eq. (1):

$$\sigma = 10 \lg \left( \frac{4\pi S}{\lambda^2} \left| \frac{E_s}{E_i} \right| \right)^2 \quad (1)$$

where  $S$ ,  $\lambda$ ,  $E_s$  and  $E_i$  represent the area of the simulation model, the wavelength of the incident wave, and the electric field strength of the transmitted wave and the received wave, respectively.

### 3 Results and discussion

#### 3.1 Composition and microstructure

The phase composition and structure of Fe/Co@C-CNFs were examined by XRD presented in Fig. 2a–c. As shown in the orange circle, they all show a weak broad diffraction peak at  $2\theta = 26^\circ$ , which corresponds to the (002) crystal plane of hexagonal graphite carbon (PDF No. 41-1487), and the presence of amorphous carbon broadens the diffraction peak of graphite carbon [25]. The  $2\theta = 44.7^\circ$ ,  $65.0^\circ$ ,  $82.3^\circ$  diffraction peaks of F4C0 are attributed to the (110), (200), (211) crystal planes of the body-centered cubic (bcc)-Fe (PDF No. 06-0696) respectively, and the other diffraction peaks are attributed to Fe<sub>3</sub>C (PDF No. 76-1877). With the increase in cobalt content, the Fe<sub>3</sub>C

diffraction peak of the composite disappears, and the main diffraction peak ( $2\theta = 44.7^\circ$ ) of F3C1 belongs to Fe, indicating that the introduction of cobalt atoms inhibits the formation of carbides. The diffraction peaks of FeCo ( $2\theta = 31.3^\circ$ ,  $44.8^\circ$ ,  $55.7^\circ$ ) were observed in F3C1, F2C2 and F1C3, corresponding to their (100), (110) and (111) crystal planes, respectively (PDF No. 44-1433). In addition, the diffraction peaks of  $2\theta = 44.2^\circ$ ,  $51.5^\circ$  and  $75.9^\circ$  in F1C3 and F0C4 are attributed to the (111), (200) and (220) crystal planes of face-centered cubic (fcc)-Co (PDF No. 15-0806), respectively. In fact, cobalt has two structural phases: fcc and hexagonal close-packed (hcp) phases, which usually coexist at room temperature and are usually difficult to separate [26]. Compared with the Joint Committee on Powder Diffraction Standards (JCPDS) database, the structure of cobalt in the synthesized nanofibers is identified as fcc-Co, but not hcp-Co. The fcc structure is a high-temperature phase of Co, which usually exists only above 420 °C. The presence of fcc-Co at room temperature may be due to the small particle nature of the material and the “quenching effect” [27]. That is to say, the formation of fcc-Co phase may be due to the presence of graphite. Metal nanoparticles are basically wrapped by ordered graphite layers, so that the fcc-Co phase can be stable at room temperature [28].

In order to further characterize the distribution of carbon in Fe/Co@C-CNFs, the samples were characterized by Raman spectroscopy as shown in Fig. 2d [29]. Fe/Co@C-CNFs show two obvious peaks at 1350 and 1580 cm<sup>-1</sup>, corresponding to D peak and G peak, respectively. By database comparison and analysis, the D peak is produced by the benzene ring vibration of amorphous carbon, which can be used to characterize the defect structure and disorder

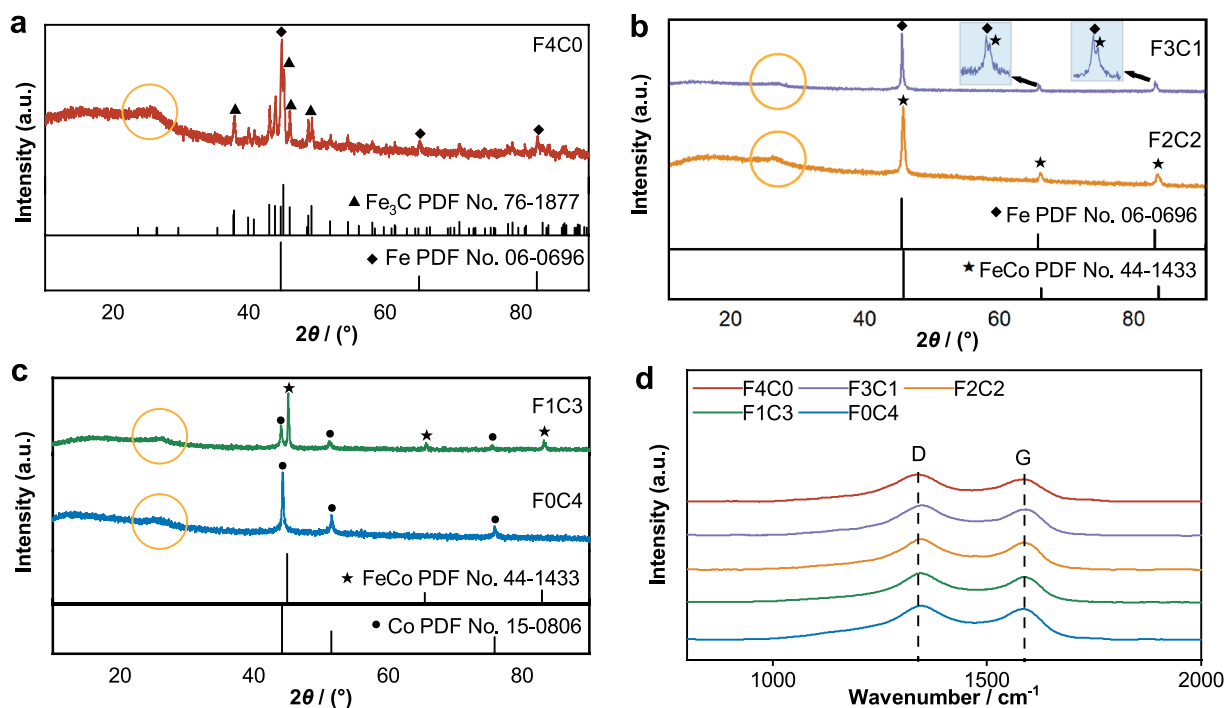


**Fig. 2** XRD patterns of **a** F4C0, **b** F3C1 and F2C2, **c** F1C3 and F0C4; **d** Raman spectra of Fe/Co@C-CNFs

degree of carbon. The G peak is generated by the stretching vibration of  $sp^2$  hybridization in graphite carbon [30–34]. The degree of graphitization of carbon materials can be determined by comparing the intensity ratio of the D peak to G peak ( $I_D/I_G$ ). In general, the high value of  $I_D/I_G$  is regarded as a low level of graphitization. The  $I_D/I_G$  values of the five samples were calculated to be 1.21, 1.16, 1.13, 1.13 and 1.11, respectively. This result shows that the degree of graphitization ( $I_D/I_G$ ) of carbon remained at a similar level. Compared with the relevant research, the  $I_D/I_G$  values of Fe/Co@C-CNFs are higher, proving that there are a lot of defects and amorphous carbon in Fe/Co@C-CNFs [35, 36].

In order to learn more about the microstructure and distribution of metal nanoparticles in Fe/Co@C-CNFs, SEM tests were performed (Fig. 3). It is evident that the 3D cross-linked fiber morphology is effectively maintained after carbonization. These fibers, whose diameter is distributed from 100 to 300 nm, interweave together to form a conductive network. The majority of magnetic nanoparticles are uniformly distributed on the surface of carbon nanofibers and come in spherical or irregular shapes. The F0C4 nanoparticles are the densest among the other groups, and as a result, their impedance matching capabilities are much improved and magnetic loss can get raised. However, in F1C3, the distribution of magnetic nanoparticles is not uniform, and carbon nanofibers have accumulated and agglomerated with

each other, making it difficult to form continuous fibers, which may affect its electromagnetic properties.

The microstructures of F2C2 and F0C4 were further characterized by selected area electron diffraction (SAED), transmission electron microscope (TEM) and high resolution transmission electron microscope (HRTEM) in Fig. 4. SAED patterns are consistent with the results of XRD patterns, indicating that the generated nanoparticles have polycrystalline properties. Obviously, the near-spherical protrusions on the nanofibers' surface could be differentiated magnetic nanoparticles that are uniformly dispersed inside or on the nanofibers' surface, with essentially no aggregation. The HRTEM image of F2C2 (Fig. 4b) proves that the near-spherical protrusions are core-shell structure, and the ordered lattice fringes are observed in the surrounding area. The interplanar spacing is 0.342 and 0.201 nm, respectively, corresponding to the (002) crystal plane of the outer graphite shell and the (110) crystal plane of the inner FeCo alloy core. A similar core-shell structure is visible in the HRTEM picture of F0C4 (Fig. 4e), with an interplanar spacing of 0.342 and 0.205 nm, respectively, corresponding to the (002) crystal plane of the outer graphite shell and the (111) crystal plane of the inner FCC-Co. However, there are still areas outside of the core-shell region that lack lattice fringes and are thought to contain amorphous carbon. Additionally, the HRTEM pictures present a lot of defects which include point defects, lattice dislocations,

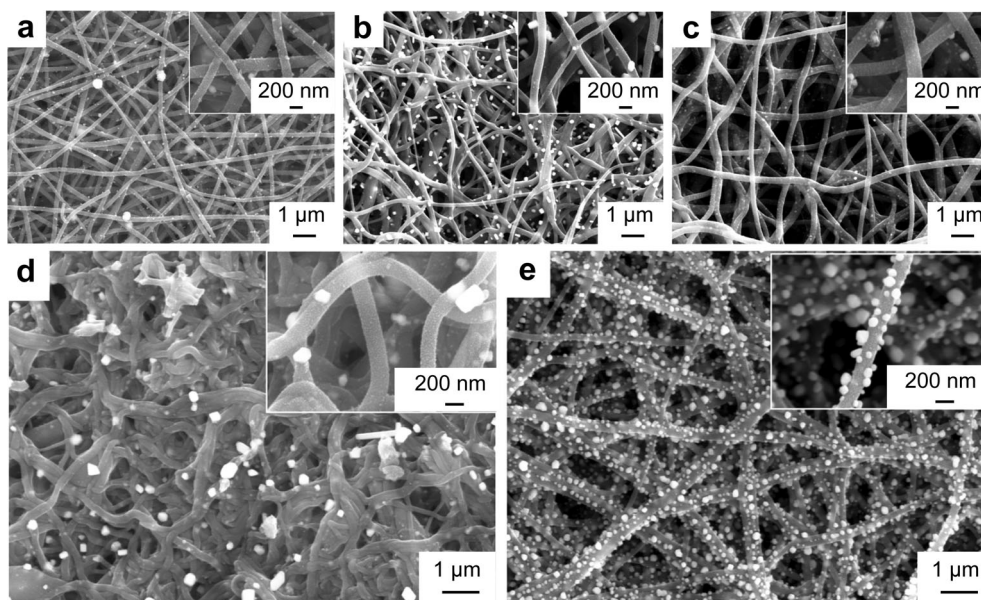


**Fig. 3** SEM images of Fe/Co@C-CNFs: **a** F4C0, **b** F3C1, **c** F2C2, **d** F1C3 and **e** F0C4

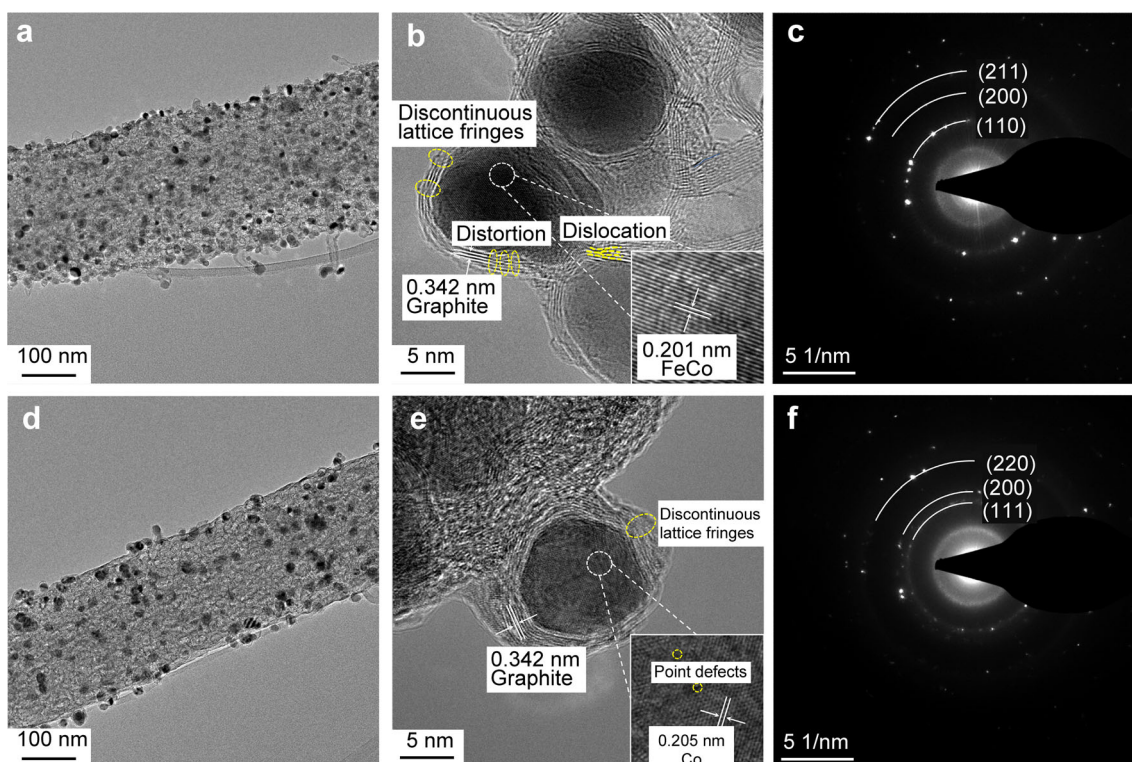


**Fig. 4** TEM, HRTEM and SAED images of **a–c** F2C2 and **d–f** F0C4

discontinuous lattice fringes and lattice distortion. These defects typically cause the lattice's periodicity to be destroyed, and electrons' hopping or capture significantly alters the electric field and electric transport pathway [37]. They can also act as polarization centers to assist in creating dipole polarization, which increases dielectric loss and

boosts the material's absorption capacity [38]. On the one hand, the advantages of this core–shell structure are reflected in the fact that the outer graphite layer and amorphous carbon can maximize the oxidation resistance and corrosion resistance of the encapsulated nanoparticles, thus effectively improving the stability of the EMW absorption performance

of Fe/Co@C-CNFs nanocomposites in various environments. On the other hand, the multiple heterogeneous interfaces between magnetic nanoparticles, interface phase, graphite, amorphous carbon, and defects can cause more interfacial polarization and multiple reflections when exposed to EMW, which helps to improve the EMW absorption performance of Fe/Co@C-CNFs.

### 3.2 Magnetic properties

In order to explore the magnetic properties of Fe/Co@C-CNFs, a vibrating sample magnetometer (VSM) was used to determine the hysteresis loop at room temperature presented in Fig. 5. The five samples all show typical soft magnetic behavior. The saturation magnetization ( $M_s$ ) of F4C0, F3C1, F2C2, F1C3 and F0C4 are 0.03374, 0.05451, 0.05200, 0.04072 and 0.03806  $\text{A}\cdot\text{m}^2\cdot\text{g}^{-1}$ , respectively, and they all saturate in the outfield at about 0.8 T. It can be seen that the saturation magnetization added with single acetylacetonate iron (F4C0) or acetylacetonate cobalt (F0C4) is relatively weak, while the saturation magnetization of F3C1, F2C2, F1C3 is higher, which is conducive to the formation of high permeability. As the mole fraction of cobalt increases, the saturation magnetization gradually decreases, mainly because the Fe atom has a relatively higher magnetic moment (compared to the Co atom) [39]. It is proved that the molar ratio of the doped Fe/Co determines the saturation magnetization, which further shows that the composites have strong magnetic loss ability.

The coercivity ( $H_c$ ) is about 0.019 T (F4C0), 0.029 T (F3C1), 0.045 T (F2C2), 0.025 T (F1C3) and 0.023 T (F0C4), respectively. The coercivity is substantially higher than that of the bulk metal, most likely as a result of the surface anisotropy field due to magnetic nanoparticles' tiny

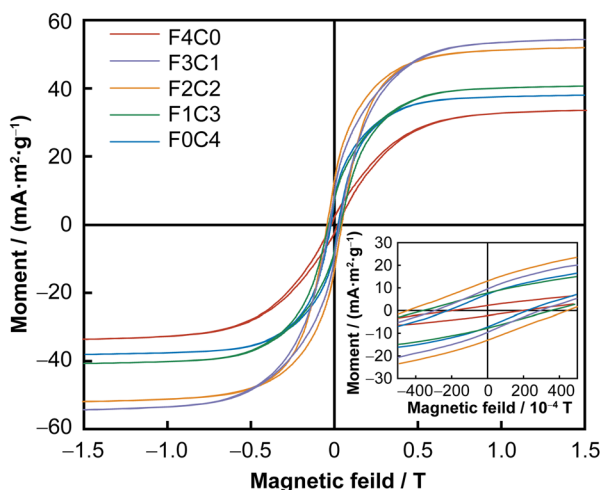


**Fig. 5** Hysteresis loop of Fe/Co@C-CNFs and details of  $M$ - $H$  curves at low applied fields

size influence [28]. In general, samples with larger  $H_c$  values may be easier to achieve high-frequency resonance and enhance absorption performance, which can be inferred that F2N2 has better absorbing properties [40].

### 3.3 Electromagnetic absorbing properties

Generally speaking, material absorption characteristics are strongly connected to electromagnetic parameters. Complex permittivity ( $\epsilon_r = \epsilon' - j\epsilon''$ ) and complex permeability ( $\mu_r = \mu' - j\mu''$ ) are two significant characteristics that determine the absorption effect in the field of EMW absorption. The real part and imaginary part of the permittivity represent the ability to store charge and dielectric loss, respectively [41, 42]. The capacity to store magnetic and magnetic loss are represented, respectively, by the real and imaginary part of the permeability [43]. The strength of the material's dielectric loss and magnetic loss can be calculated using the ratio of the imaginary part to the real part of its permittivity and permeability ( $\tan\delta_\epsilon = \epsilon''/\epsilon'$  and  $\tan\delta_\mu = \mu''/\mu'$ ) [44].

The complex permittivity and complex permeability of the material were measured in 2–18 GHz. As can be seen from Fig. 6a, b, the real part and imaginary part of the permittivity exhibit dispersion characteristics throughout the test frequency band, i.e., decrease with the increase of frequency, which is due to the dipole polarization [45]. The imaginary part of the permittivity shows slight peaks in the test frequency band, which is related to the dielectric resonance [46]. It is observed that the  $\epsilon''$  of F4C0 is much larger than that of F1C3, which is speculated to be due to the high conductivity of F4C0 with good continuous carbon nanofibers and the low conductivity of F1C3 caused by the accumulation of carbon fiber clusters, the destruction of the electron migration path and the formation of less conductive network. What's more,  $\epsilon''$  is positively correlated with the conductivity based on the free electron theory (Eq. (2)), so the  $\epsilon''$  of F1C3 is much lower [37].

$$\epsilon_c'' = \frac{\sigma}{\epsilon_0\omega} \quad (2)$$

In order to further prove the different dielectric loss mechanisms in Fe/Co@C-CNFs, the loss mechanism was analyzed by Debye theory. The equations of this theory are as follows [47, 48]:

$$\epsilon' = \frac{\epsilon_s - \epsilon_\infty}{1 + \omega^2\tau^2} + \epsilon_\infty \quad (3)$$

$$\epsilon'' = \epsilon_p'' + \epsilon_c'' = \omega\tau \frac{\epsilon_s - \epsilon_\infty}{1 + \omega^2\tau^2} + \frac{\sigma}{\epsilon_0\omega} \quad (4)$$

where  $\epsilon_s$  and  $\epsilon_\infty$  are the permittivity under electrostatic field and high frequency, respectively;  $\omega$  is angular frequency;  $\tau$  is the relaxation time related to frequency and temperature;  $\epsilon_0$  is

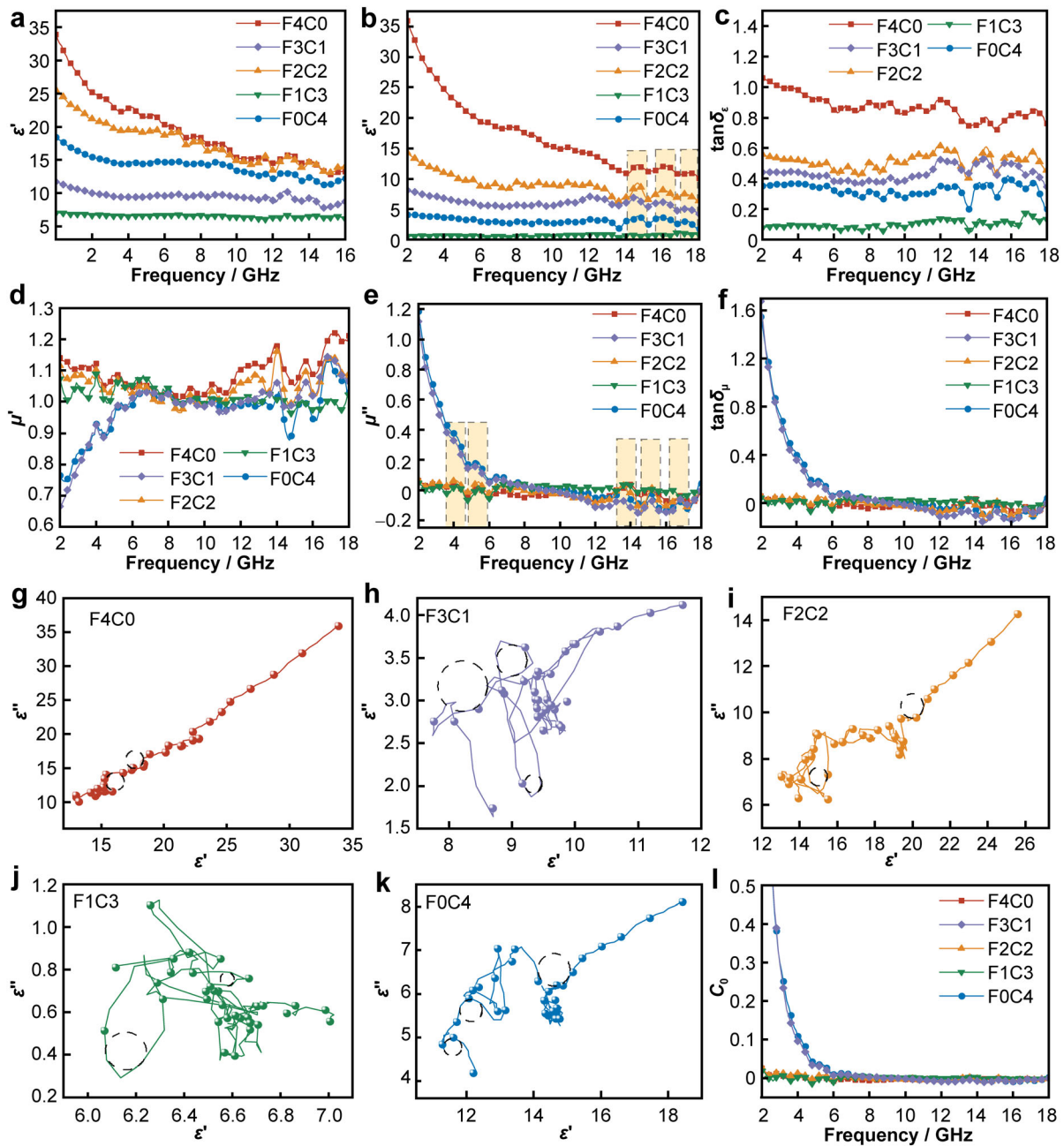


**Fig. 6** **a, b** Complex permittivity and **d, e** complex permeability as well as **c** dielectric and **f** magnetic loss tangent for Fe/Co@C-CNFs; Cole–Cole graphs of **g** F4C0, **h** F3C1, **i** F2C2, **j** F1C3 and **k** F0C4; **l**  $C_v$  of Fe/Co@C-CNFs

the dielectric constant of free space;  $\epsilon_p''$  and  $\epsilon_c''$  are polarization loss and conductivity loss, respectively. Polarization loss refers to the relaxation phenomenon in the “aggregation-dispersion” process of charge or the “orientation-deorientation” process of polarization sites on various heterostructures. However, the conductivity loss typically occurs on the local microcurrent network when aggregation-induced charge transportation is stimulated by alternating

electromagnetic fields [49]. According to the above equations, the  $\epsilon''$  of F4C0 decreases significantly with the increase of frequency, indicating that it is dominated by conductivity loss. This is due to the interlaced connection of the composite fibers stimulating the structure of the conductive network and the electronic transition at the fiber junction increasing conductivity loss. Since the changing trend of the other groups'  $\epsilon''$  is not obvious, it is

assumed that the loss is a combination of conductivity loss and polarization loss. Combine Eqs. (3) and (4) to get Eq. (5) [50, 51]:

$$\left(\varepsilon' - \frac{\varepsilon_s - \varepsilon_\infty}{2}\right)^2 + (\varepsilon'')^2 = \left(\frac{\varepsilon_s - \varepsilon_\infty}{2}\right)^2 \quad (5)$$

It is clear that the graph obtained from Eq. (5) is a semicircle, which is called Cole–Cole graph (Fig. 6j, k). Each polarization relaxation process corresponds to a semicircle. In particular, the Cole–Cole curves of F4C0 and F1C3 are particularly different: most part of the Cole–Cole curve of the former is similar to straight lines, indicating that the main loss is conductive loss and the conductivity is high; in the latter, no straight line-like part is observed, which proves that its conductivity is not good and there is almost no conductive loss [52]. This confirms the speculation that their large difference of  $\varepsilon''$  depends mostly on their conductivity. However, the existence of multiple semicircles in the Cole–Cole plots indicates the presence of multiple polarization loss. Traditionally, the polarization includes ion polarization, electron polarization, dipole polarization and heterogeneous interface polarization. However, the ion polarization and electron polarization are not considered here, because the corresponding relaxation frequency ( $10^3$ – $10^6$  GHz) is much higher than the microwave frequency. Therefore, the polarization relaxation loss (2–18 GHz) can be mainly attributed to dipole polarization and interface polarization [49]. Fe/Co@C-CNFs composites have non-uniform charge distribution and dipole polarization centers due to the destruction of the graphite lattice by magnetic nanoparticles. Additionally, the numerous heterogeneous interfaces between magnetic nanoparticles, interfacial phase, amorphous carbon, paraffin and core–shell Fe/Co@C can produce significant interface polarization loss [53–55]. That is to say, the electromagnetic energy will therefore be converted into thermal energy for further attenuation by the periodic repeating reaction of these polarization centers [37].

The frequency dependence of the real part and imaginary part of complex permeability and magnetic loss tangent of Fe/Co@C-CNFs are presented in Fig. 6d–f. Due to the existence of magnetic nanoparticles, magnetic loss becomes another quite important factor influencing the EMW absorption effect. The curves of  $\tan\delta_\mu$  value of F4C0, F2C2 and F1C3 are consistent with the trend of the imaginary part of the permeability curve while the value fluctuates between  $-0.1$  and  $0.2$ . F3C1 and F0C4, however, they decrease rapidly in the range of 2–5 GHz. It is well known that the magnetic loss in the 2–18 GHz band is mainly due to eddy current effect, natural resonance and exchange resonance [56]. The eddy current loss can be characterized by  $C_0$  value  $C_0 = \mu''(\mu')^{-2}f^{-1}$  [57]. If the

magnetic loss is derived from the eddy current effect, then the value of  $C_0$  should remain near a constant with the change of frequency. As shown in Fig. 6l,  $C_0$  fluctuates very little in 5–18 GHz, which infers that the magnetic loss of the material in this frequency band is mainly from the eddy current effect. The values of  $C_0$  of F3C1 and F0C4 vary greatly with frequency in 2–5 GHz, so natural resonance and exchange resonance may take the upper hand in this frequency bands. The natural resonance frequency can be determined by the following formula [58].

$$2\pi f_r = rH_a \quad (6)$$

$$H_a = 4|K_1|/3\mu_0M_s \quad (7)$$

where  $f_r$  is the natural resonance frequency,  $H_a$  denotes the anisotropy field,  $r$  denotes the gyromagnetic ratio, and  $K_1$  is the anisotropy coefficient. Calculated by this formula, the natural resonance frequency is usually between 2 and 10 GHz. Additionally, exchange resonance always occurs in higher frequency bands (10–18 GHz) [49]. Therefore, it can be deduced that the magnetic loss of F3C1 and F0C4 diminishes significantly more quickly in the 2–5 GHz range due to natural resonance, whereas the magnetic loss in the 5–18 GHz range is mostly caused by eddy current loss. Three weak peaks can also be observed in the graph of  $\mu''$  in 13–16 GHz range which are attributed to the exchange resonance, while two peaks in 3–6 GHz range reveal the natural resonance.

Based on the theory of EMW transmission lines, the impedance of free space is represented by  $Z_0$  ( $Z_0 = 376.7 \Omega$ ) and the impedance of dielectric material surface is represented by  $Z_{in}$  for infinite thick (or enough thick) plane absorbing material. The RL can be obtained as follows[59]:

$$RL = 20\lg \left| \frac{Z_{in} - Z_0}{Z_{in} + Z_0} \right| \quad (8)$$

3D, 2D and 1D reflection loss graphs were created to assess the EMW absorption capabilities in Figs. 7, S1. In general,  $RL = -10$  dB means that 90% of EMW is absorbed. The  $RL < -10$  dB band range is called EAB. From Fig. S1a, b, it can be seen clearly that the RL of F4C0 is higher than  $-10$  dB, so there is almost no absorbing performance. From Fig. 7, however, the minimum RL of F3C1/F2C2/F1C3/F0C4 is  $-50.70$  dB/ $-18.66$  dB/ $-14.36$  dB/ $-48.28$  dB when the thickness of the absorber is 4.26 mm/1.08 mm/5.00 mm/1.32 mm, respectively. When the thickness is 4.68 mm/1.22 mm/5.00 mm/1.41 mm, the maximum EAB is 3.4 GHz (4.7–6.1 GHz and 15.3–17.1 GHz)/4.2 GHz (13.9–18 GHz)/0.8 GHz (17.3–18 GHz)/4.1 GHz (13.3–17.3 GHz), respectively. Overall, F2C2 has better absorption performance, which can achieve stronger and wider absorption effect in a thinner thickness. In Table 1, the EMW absorption properties of Fe/Co@C-



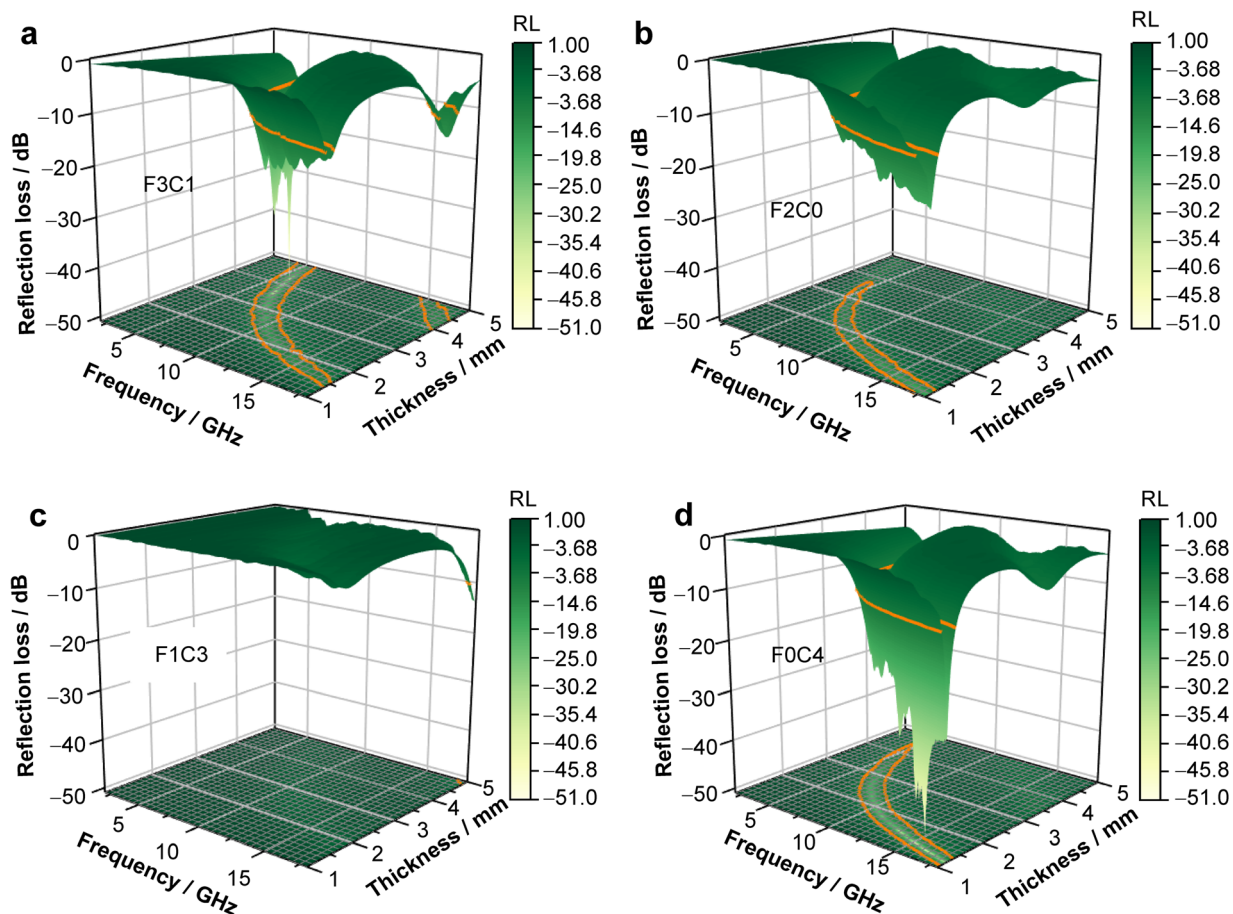


**Fig. 7** 3D reflection loss graphs: **a** F3C1, **b** F2C2, **c** F1C3 and **d** F0C4

**Table 1** Comparison of EMW absorption properties of carbon nanofibers prepared by electrospinning

Samples	Filler loading / wt%	Minimum RL values		$RL < -10$ dB		Refs.
		$RL_{\min}$ / dB	Matching thickness / mm	$d$ / mm	EAB <sub>max</sub> / GHz	
Ni/MnO-CNFs	15	-53.23	2.30	2.90	6.50	[47]
CoFe <sub>2</sub> O <sub>4</sub> /FeCo-CNFs	50	-38.10	2.50	–	4.10	[60]
Ni/NiO-CNFs	10	-47.90	3.00	2.55	4.50	[61]
C/SiO <sub>2</sub> @Fe/Co-CNFs	30	-59.60	1.43	–	4.60	[62]
FeNi-CNFs	30	-24.80	2.70	1.80	4.40	[63]
CNFs	10	-12.75	2.20	2.40	5.04	[64]
F2C2	15	-18.66	1.08	1.22	4.20	This work

CNFs are compared with those of other nanocomposites studied recently, which reveals that this work has the benefit that it realizes a relatively wide EAB (4.20 GHz) at a very thin thickness (1.22 mm). This offers a fresh thought for the development of lightweight high-performance microwave absorbers [47, 60–64].

Impedance matching characteristic (Fig. 8a–e) is an important factor for absorbing ability of materials, which determines whether EMW can enter the interior of absorbing materials. The impedance matching  $Z_r$  can be calculated by Eq. (9), where  $f$  represents the frequency,  $c$  is the propagation velocity of light in vacuum, and

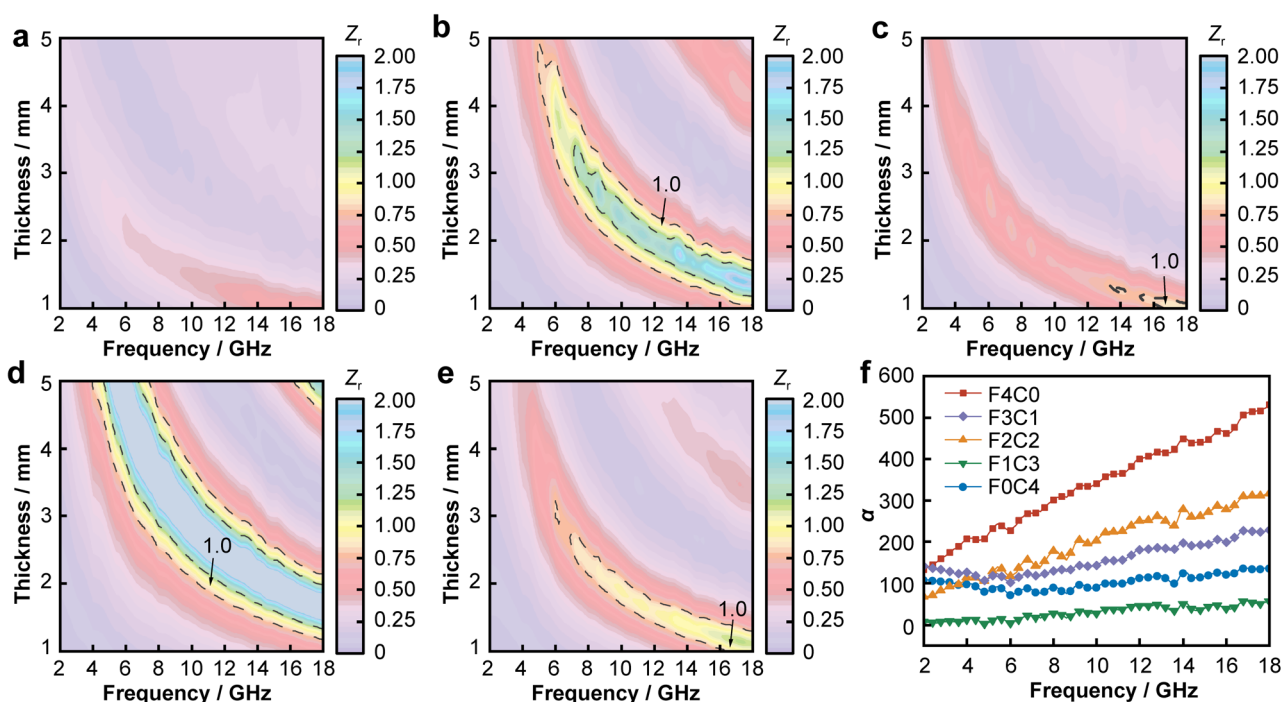


**Fig. 8** Impedance matching diagrams: **a** F4C0, **b** F3C1, **c** F2C2, **d** F1C3 and **e** F0C4; **f** plots of attenuation constant

$d$  represents the thickness of the absorbing material [65, 66].

$$Z_r = Z_{in}/Z_0 = \sqrt{\frac{\mu_r}{\varepsilon_r}} \tanh\left(\frac{2\pi f d}{c} \sqrt{\frac{\mu_r}{\varepsilon_r}}\right) \quad (9)$$

In general, the closer the value of  $Z_r$  is to 1, the closer the material's surface impedance is to the impedance of air, and the easier it is for EMW to enter the interior of the absorbing material without reflections [67]. It can be concluded that when the thickness of the absorber is relatively thin, the area with better impedance matching of the sample is mainly concentrated in the high frequency stage. The area between the dotted lines represents the  $Z_r$  value between 0.8 and 1.2. It is clear that even if F4C0 has high dielectric properties, the  $Z_r$  value deviates from 1.0, which is the most important reason why its absorbing property is poor. Moderate dielectric qualities are therefore crucial in the design of absorption materials since either high or low dielectric characteristics can result in impedance mismatch [68]. In contrast, the area of  $Z_r$  between 0.8 and 1.2 of F3C1, F1C3 and F0C4 is relatively large, which indicates that these groups can mostly achieve the effect of making more EMW enter the material with little reflection at a low thickness. F3C1, F1C3 and F0C4 have good impedance matching but cannot obtain better EMW absorption, which is attributed to another factor affecting EMW absorption, namely attenuation characteristic ( $\alpha$ ). It determines the absorbing ability of materials calculated by Eq. (10) [69, 70].

$$\alpha = \frac{\sqrt{2}\pi f}{c} \sqrt{(\mu''\varepsilon'' - \mu'\varepsilon') + \sqrt{(\mu''\varepsilon'' - \mu'\varepsilon')^2 + (\mu'\varepsilon'' - \mu''\varepsilon')^2}} \quad (10)$$

Figure 8f illustrates the increasing attenuation constant of the material with frequency, especially at high frequency. The attenuation constant of F4C0 is significantly larger than those of the other four samples, which may result from its high  $\varepsilon''$ , suggesting that it has the best EMW attenuation ability. The above analysis shows that although the attenuation constant of F4C0 is the largest, its absorbing performance is not good, which further shows that the absorbing performance is determined by not only electromagnetic attenuation characteristics but also impedance matching.

Based on the above discussion, the EMW absorption mechanism of Fe/Co@C-CNFs is proposed as shown in Fig. 9. First, on a macroscale, embedding magnetic nanoparticles improves impedance matching, ensuring that EMW can efficiently enter the interior of absorbing materials. Secondly, on the mesoscopic scale, the multiple heterogeneous interfaces between magnetic nanoparticles, interface phase, graphite, amorphous carbon, defects and paraffin cause multiple reflections and absorption of EMW, which enhances the absorbing ability. The 3D cross-linked network structure of the composite material also increases the reflection of the EMW between the fibers, expands the propagation path, and improves the opportunity for the EMW to be absorbed by the composite materials. Finally,

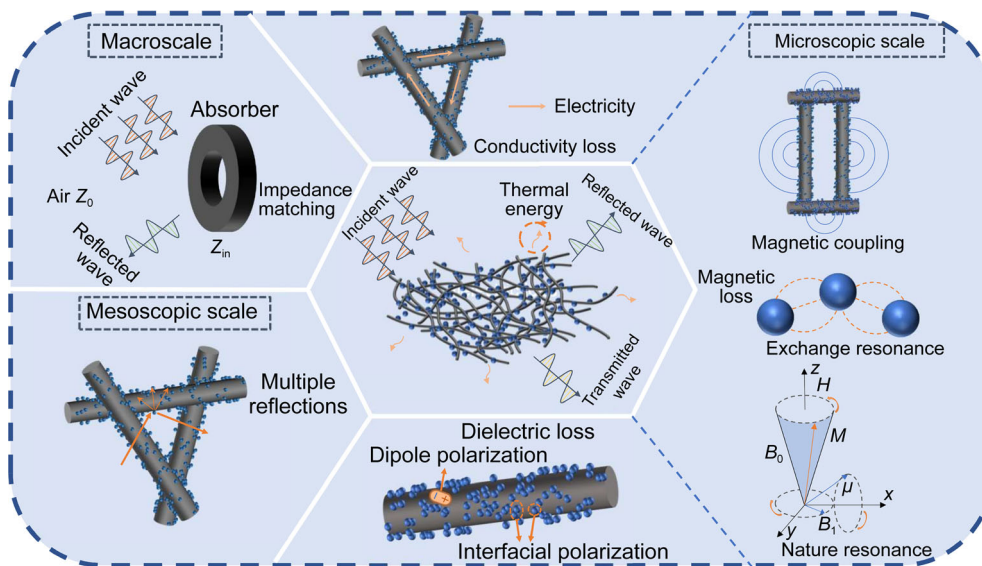


Fig. 9 EMW absorption mechanism of Fe/Co@C-CNFs

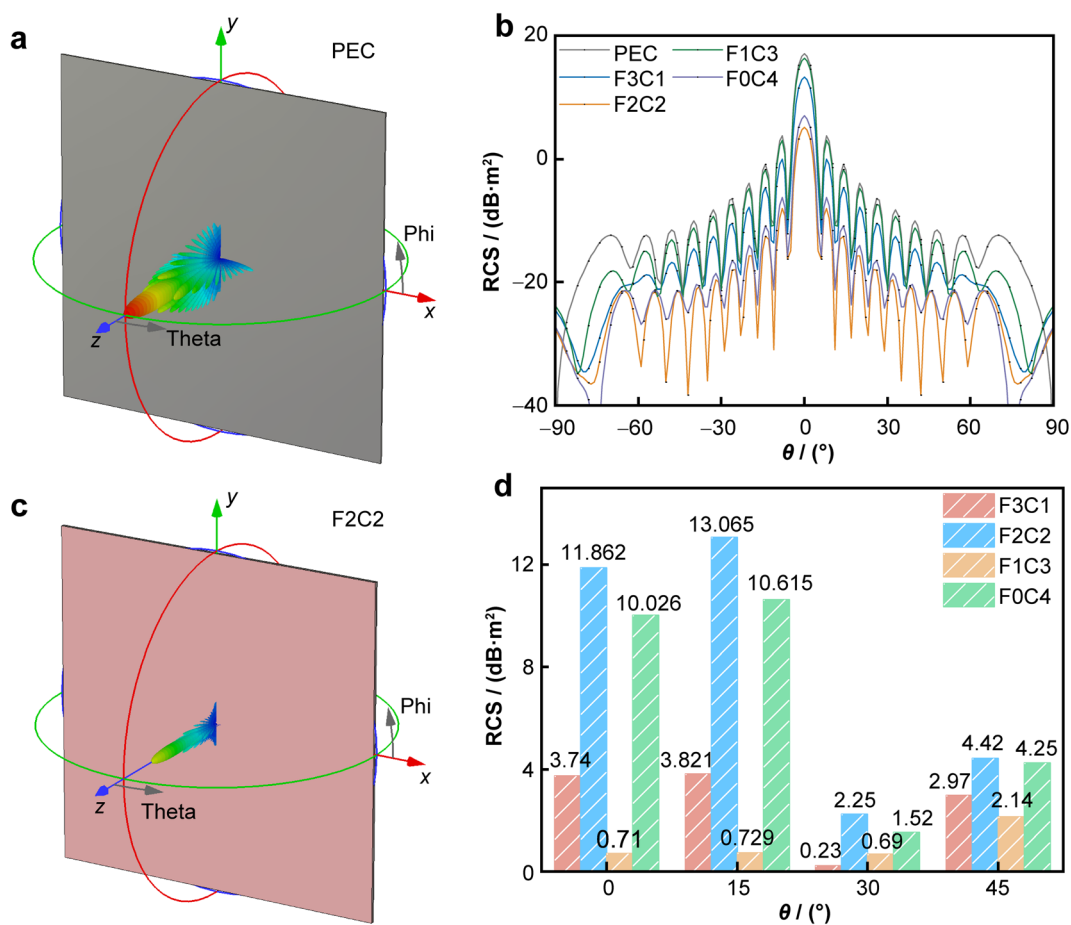


Fig. 10 3D RCS images for PEC substrate with a no cover and c F2C2 coating; b 1D RCS plots in angle range from - 90° to + 90°; d RCS reduction achieved from subtracting composite with PEC

at the microscopic scale, the electron migration and hopping in the 3D conductive network composed of Fe/Co@C-CNFs generate a distributed microcurrent; moreover, the magnetic nanoparticles loaded on the fiber surface improve the conductivity of the fiber and enhance the conductive loss. The strong dielectric loss is mainly derived from dipole polarization and interface polarization. The former is mainly due to the destruction of graphite lattice by magnetic nanoparticles, resulting in uneven charge distribution as well as various structural defects and functional groups, while the latter is caused by multiple heterogeneous interfaces. Magnetic loss is primarily caused by natural and exchange resonance, as well as eddy current loss, which is primarily caused by magnetic particles.

### 3.4 RCS simulation results

Absorbers are often coated on the surface of the substrate to reduce the far-field RCS. In order to test the actual performance of Fe/Co@C-CNFs, the CST studio suite was used to model PEC substrate with a size of 100 mm × 100 mm × 1 mm and coated with 1.22 mm of F3C1, F2C2, F1C3 and F0C4 coating, respectively [71]. When at 15 GHz and  $\varphi = 0^\circ$ , Fig. 10a, c shows 3D RCS of the uncoated PEC substrate and the substrate coated with F2C2, respectively, demonstrating that the far-field RCS of the latter is significantly reduced compared with the former. In order to quantify the specific RCS reduction, Fig. 10b, d gives the 1D RCS plots in the angle range from  $-90^\circ$  to  $+90^\circ$  and the RCS reduction compared with PEC at  $0^\circ$ ,  $15^\circ$ ,  $30^\circ$  and  $45^\circ$ , respectively. Each group has different contributions to RCS reduction. Especially at  $\theta = 15^\circ$ , the contributions of F3C1, F2C2, F1C3 and F0C4 to RCS reduction reach 3.821, 13.065, 0.729 and 10.615 dB·m<sup>2</sup>, respectively. At all detection angles, the RCS reduction value of F2C2 coating is much larger than that of the other three coatings (11.862, 13.065, 2.25 and 4.42 dB·m<sup>2</sup> at  $0^\circ$ ,  $15^\circ$ ,  $30^\circ$  and  $45^\circ$ ), which confirms the conclusion that F2C2 has the best absorbing performance from another point of view. Fe/Co@C-CNFs are obviously successful in reducing RCS, which has significant practical implications for the development of lightweight high-performance absorbers.

## 4 Conclusion

In this paper, carbon nanofibers embedded with Fe-Co alloy nanoparticles were prepared by electrospinning and a high temperature pyrolysis carbonization process. The prepared carbon nanofibers exhibit a 3D cross-linked network structure, and the magnetic nanoparticles are evenly distributed on their surface. The core-shell structure

formed by the magnetic nanoparticles and graphite lays a foundation for the stable performance of the absorbers. Better absorption qualities can be found in F2C2: the minimum RL of F2C2 is  $-18.66$  GHz at 1.08 mm thick, and the maximum EAB is 4.2 GHz (13.9–18 GHz). The EMW loss mechanism mainly includes appropriate impedance matching, strong conductivity loss, dielectric loss and magnetic loss. By CST simulating verification, the RCS reduction results of F2C2 coating contribute up to 11.862, 13.065, 2.25 and 4.42 dB·m<sup>2</sup> at  $0^\circ$ ,  $15^\circ$ ,  $30^\circ$  and  $45^\circ$ , respectively. This work exemplifies a superior design strategy for 3D networked carbon nanofibers embedded with Fe-Co alloy nanoparticle systems, shedding light on the future synthesis of lightweight, high-performance EMW absorbers, which have great application potential in energy storage and energy conversion.

**Acknowledgements** This work was financially supported by the National Natural Science Foundation of China (No. 52272117), the National Key Research and Development Program of China (Nos. 2022YFB3505104 and 2022YFB3706604) and the Key Research and Development Program of Shandong Province (No. 2022TSGC2322). The authors would like to thank Shiyanjia Lab ([www.shiyanjia.com](http://www.shiyanjia.com)) for the support of TEM/HRTEM/SAED tests.

### Declarations

**Conflict of interests** The authors declare that they have no conflict of interest.

## References

- [1] Zhao B, Bai ZY, Lv HL, Yan ZK, Du Y, Guo XQ, Zhang JC, Wu LM, Deng JS, Zhang DW, Che RC. Self-healing liquid metal magnetic hydrogels for smart feedback sensors and high-performance electromagnetic shielding. *Nano-Micro Lett.* 2023;15(1):79. <https://doi.org/10.1007/s40820-023-01043-3>.
- [2] Zhang ZD, Zhao YM, Fan GH, Zhang WJ, Liu Y, Liu JR, Fan RH. Paper-based flexible metamaterial for microwave applications. *EPJ Appl Metamater.* 2021;8:6. <https://doi.org/10.1051/epjam/2020016>.
- [3] Zhao B, Li Y, Zeng QW, Wang L, Ding JJ, Zhang R, Che RC. Galvanic replacement reaction involving core-shell magnetic chains and orientation-tunable microwave absorption properties. *Small.* 2020;16(40):2003502. <https://doi.org/10.1002/sml.202003502>.
- [4] Wang BL, Wu Q, Fu YG, Liu T. A review on carbon/magnetic metal composites for microwave absorption. *J Mater Sci Technol.* 2021;86:91. <https://doi.org/10.1016/j.jmst.2020.12.078>.
- [5] Qi GY, Liu Y, Chen LL, Xie PT, Pan D, Shi ZC, Quan B, Zhong YM, Liu CZ, Fan RH, Guo ZH. Lightweight Fe<sub>3</sub>C@Fe/C nanocomposites derived from wasted cornstalks with high-efficiency microwave absorption and ultrathin thickness. *Adv Compos Hybrid Mater.* 2021;4(4):1226. <https://doi.org/10.1007/s42114-021-00368-0>.
- [6] Zhang HY, Li JY, Pan Y, Liu YF, Mahmood N, Jian X. Flexible carbon fiber-based composites for electromagnetic interference shielding. *Rare Met.* 2022;41(11):3612. <https://doi.org/10.1007/s12598-022-02057-3>.
- [7] Zhang J, Shao LD, Li ZF, Zhang CB, Zhu WR. Graphene-based optically transparent metasurface capable of dual-polarized

- modulation for electromagnetic stealth. *ACS Appl Mater Interfaces*. 2022;14(27):31075. <https://doi.org/10.1021/acami.2c04414>.
- [8] Lan D, Qin M, Liu JL, Wu GL, Zhang Y, Wu HJ. Novel binary cobalt nickel oxide hollowed-out spheres for electromagnetic absorption applications. *Chem Eng J*. 2020;382: 122797. <https://doi.org/10.1016/j.cej.2019.122797>.
- [9] Xie PT, Liu Y, Feng M, Niu M, Liu CZ, Wu NN, Sui KY, Patil RR, Pan D, Guo ZH, Fan RH. Hierarchically porous Co/C nanocomposites for ultralight high-performance microwave absorption. *Adv Compos Hybrid Mater*. 2021;4(1):173. <https://doi.org/10.1007/s42114-020-00202-z>.
- [10] Huidobro PA, Maier SA, Pendry JB. Tunable plasmonic metasurface for perfect absorption. *EPJ Appl Metamater*. 2017;4:6. <https://doi.org/10.1051/epjam/2017001>.
- [11] Lu C, Mei ZL, Tang WX, Cui TJ. Manipulating scattering features by metamaterials. *EPJ Appl Metamater*. 2016;3:3. <https://doi.org/10.1051/epjam/2016005>.
- [12] Chen X, Wang YQ, Guo Z, Wu X, Yang FQ, Sun Y, Li Y, Jiang HT, Chen H. Significant enhancement of magnetic shielding effect by using the composite metamaterial composed of mu-near-zero media and ferrite. *EPJ Appl Metamater*. 2021;8: 13. <https://doi.org/10.1051/epjam/2021008>.
- [13] Wang YM, Li TX, Zhao LF, Hu ZW, Gu YJ. Research progress on nanostructured radar absorbing materials. *Energy Power Eng*. 2011;03:580. <https://doi.org/10.4236/epe.2011.34072>.
- [14] Liu PB, Gao S, Wang Y, Huang Y, He WJ, Huang WH, Luo JH. Carbon nanocages with N-doped carbon inner shell and Co/N-doped carbon outer shell as electromagnetic wave absorption materials. *Chem Eng J*. 2020;381:122653. <https://doi.org/10.1016/j.cej.2019.122653>.
- [15] Zhao B, Liang LY, Bai ZY, Guo XQ, Zhang R, Jiang QL, Guo ZH. Poly(vinylidene fluoride)/Cu@Ni anchored reduced-graphene oxide composite films with folding movement to boost microwave absorption properties. *ES Energy Environ*. 2021;14: 79. <https://doi.org/10.30919/esee8c488>.
- [16] Han MR, Yang YF, Liu W, Zeng ZH, Liu JR. Recent advance in three-dimensional porous carbon materials for electromagnetic wave absorption. *Sci China Mater*. 2022;65(11):2911. <https://doi.org/10.1007/s40843-022-2153-7>.
- [17] Zheng H, Nan K, Lu Z, Wang N, Wang Y. Core-shell FeCo@carbon nanocages encapsulated in biomass-derived carbon aerogel: Architecture design and interface engineering of lightweight, anti-corrosion and superior microwave absorption. *J Colloid Interface Sci*. 2023;646:555. <https://doi.org/10.1016/j.jcis.2023.05.076>.
- [18] Wu C, Wang J, Zhang XH, Kang L, Cao X, Zhang YY, Niu YT, Yu YY, Fu HL, Shen Z, Wu KJ, Yong Z, Zou JY, Wang B, Chen Z, Yang ZP, Li QW. Hollow gradient-structured iron-anchored carbon nanospheres for enhanced electromagnetic wave absorption. *Nano-Micro Lett*. 2022;15(1):7. <https://doi.org/10.1007/s40820-022-00963-w>.
- [19] Du YC, Liu WW, Qiang R, Wang Y, Han XJ, Ma J, Xu P, et al. Shell thickness-dependent microwave absorption of core-shell Fe<sub>3</sub>O<sub>4</sub>@C composites. *ACS Appl Mater Interfaces*. 2014;6: 12997. <https://doi.org/10.1021/am502910d>.
- [20] Park KY, Han JH, Lee SB, Kim JB, Yi JW, Lee SK. Fabrication and electromagnetic characteristics of microwave absorbers containing carbon nanofibers and NiFe particles. *Compos Sci Technol*. 2009; 69(7):1271. <https://doi.org/10.1016/j.compscitech.2009.02.033>.
- [21] Li JS, Huang H, Zhou YJ, Zhang CY, Li ZT. Research progress of graphene-based microwave absorbing materials in the last decade. *J Mater Res*. 2017;32(7):1213. <https://doi.org/10.1557/jmr.2017.80>.
- [22] Zhang SL, Qi ZW, Zhao Y, Jiao Q, Ni X, Wang YJ, Chang Y, Ding C. Core/shell structured composites of hollow spherical CoFe<sub>2</sub>O<sub>4</sub> and CNTs as absorbing materials. *J Alloys Compd*. 2017;694:309. <https://doi.org/10.1016/j.jallcom.2016.09.324>.
- [23] Wang FY, Sun YQ, Li DR, Zhong B, Wu ZG, Zuo SY, Yan D, Zhuo RF, Feng JJ, Yan PX. Microwave absorption properties of 3D cross-linked Fe/C porous nanofibers prepared by electrospinning. *Carbon*. 2018;134:264. <https://doi.org/10.1016/j.carbon.2018.03.081>.
- [24] Liu ZX, Zhang LJ, Zhao YH, Bi XR, Cai WJ, Tan LW, Liu Y, Liu D, Zhang ZD. Fe@Fe<sub>3</sub>C core-shell nanoparticles embedded in polyvinyl alcohol-derived porous carbon toward light and high-performance microwave absorption. *ECS J Solid State Sci Technol*. 2022; 11(10): 101003. <https://doi.org/10.1149/2162-8777/ac96a3>.
- [25] An Y, Qin JY, Sun K, Tian JH, Wang ZY, Zhao Y, Li XF, Fan RH. Carbon fiber skeleton/silver nanowires composites with tunable negative permittivity behavior. *EPJ Appl Metamater*. 2021;8:1. <https://doi.org/10.1051/epjam/2020019>.
- [26] Gubin SP, Spichkin YuI, Koksharov YuA, Yurkov GY, Kozinkin AV, Nedoseikina TI, Korobov MS, Tishin AM. Magnetic and structural properties of Co nanoparticles in a polymeric matrix. *J Magn Magn Mater*. 2003;265(2):234. [https://doi.org/10.1016/S0304-8853\(03\)00271-3](https://doi.org/10.1016/S0304-8853(03)00271-3).
- [27] Tomita S, Hikita M, Fujii M, Hayashi S, Akamatsu K, Deki S, Yasuda H. Formation of Co filled carbon nanocapsules by metal-template graphitization of diamond nanoparticles. *J Appl Phys*. 2000;88(9):5452. <https://doi.org/10.1063/1.1317242>.
- [28] Xiang J, Li JL, Zhang XH, Ye Q, Xu JH, Shen XQ. Magnetic carbon nanofibers containing uniformly dispersed Fe/Co/Ni nanoparticles as stable and high-performance electromagnetic wave absorbers. *J Mater Chem A*. 2014;2(40):16905.
- [29] Izadshenas S, Maslowski P, Herr T, Slowik K. Multiresonant metasurface for Raman spectroscopy beyond single molecule detection level. *EPJ Appl Metamater*. 2022;9:11. <https://doi.org/10.1051/epjam/2022009>.
- [30] Yin YC, Liu XF, Wei XJ, Yu RH, Shui JL. Porous CNTs/Co composite derived from zeolitic imidazolate framework: a lightweight, ultrathin, and highly efficient electromagnetic wave absorber. *ACS Appl Mater Interfaces*. 2016;8(50):34686. <https://doi.org/10.1021/acami.6b12178>.
- [31] Fan GH, Jiang YL, Hou CX, Deng XR, Liu ZX, Zhang LJ, Zhang ZD, Fan RH. Extremely facile and green synthesis of magnetic carbon composites drawn from natural bulrush for electromagnetic wave absorbing. *J Alloys Compd*. 2020;835: 155345. <https://doi.org/10.1016/j.jallcom.2020.155345>.
- [32] Zhao YY, Yang XB, Yan LL, Bai YP, Li SW, Sorokin P, Shao L. Biomimetic nanoparticle-engineered superwetttable membranes for efficient oil/water separation. *J Membr Sci*. 2021;618: 118525. <https://doi.org/10.1016/j.memsci.2020.118525>.
- [33] Yin Y, Jiang B, Zhu XF, Meng LH, Huang YD. Investigation of thermostability of modified graphene oxide/methylsilicone resin nanocomposites. *Eng Sci*. 2018;5(7):73. <https://doi.org/10.30919/es8d762>.
- [34] Wang ZX, Li XF, Wang LY, Li YP, Qin JY, Xie PT, Qu YP, Sun K, Fan RH. Flexible multi-walled carbon nanotubes/polydimethylsiloxane membranous composites toward high-permittivity performance. *Adv Compos Hybrid Mater*. 2020;3(1):1. <https://doi.org/10.1007/s42114-020-00144-6>.
- [35] Wu NN, Xu DM, Wang Z, Wang F, Liu JR, Liu W, Shao Q, Liu H, Gao Q, Guo ZH. Achieving superior electromagnetic wave absorbers through the novel metal-organic frameworks derived magnetic porous carbon nanorods. *Carbon*. 2019;145:433. <https://doi.org/10.1016/j.carbon.2019.01.028>.
- [36] Deng WB, Li TH, Li H, Liu X, Dang AL, Liu Y, Wu HJ. Controllable graphitization degree of carbon foam bulk toward electromagnetic wave attenuation loss behavior. *J Colloid Interface Sci*. 2022;618:129. <https://doi.org/10.1016/j.jcis.2022.03.071>.



- [37] Deng WB, Li TH, Li H, Dang AL, Liu X, Zhai JH, Wu HJ. Morphology modulated defects engineering from MnO<sub>2</sub> supported on carbon foam toward excellent electromagnetic wave absorption. *Carbon*. 2023;206:192. <https://doi.org/10.1016/j.carbon.2023.02.039>.
- [38] Yang ML, Yuan Y, Li Y, Sun XX, Wang S, Liang L, Ning YH, Li JJ, Yin W, Che RC, Li YB. Dramatically enhanced electromagnetic wave absorption of hierarchical CNT/Co/C fiber derived from cotton and metal-organic-framework. *Carbon*. 2020;161:517. <https://doi.org/10.1016/j.carbon.2020.01.073>.
- [39] Zhang CL, Nie YG, Shi HF, Ye EJ, Zhao JQ, Han ZD, Xuan HC, Wang DH. Tunable magnetostructural coupling and large magnetocaloric effect in Mn<sub>1-x</sub>Ni<sub>1-x</sub>Fe<sub>2x</sub>Si<sub>1-x</sub>Ga<sub>x</sub>. *J Magn Magn Mater*. 2017;432:527. <https://doi.org/10.1016/j.jmmm.2017.02.046>.
- [40] Liu PJ, Yao ZJ, Zhou JT, Yang ZH, Kong LB. Small magnetic Co-doped NiZn ferrite/graphene nanocomposites and their dual-region microwave absorption performance. *J Mater Chem C*. 2016;4(41):9738. <https://doi.org/10.1039/C6TC03518C>.
- [41] Zhao B, Yan ZK, Du YQ, Rao LJ, Chen GY, Wu YY, Yang LT, Zhang JC, Wu LM, Zhang DW, Che RC. High-entropy enhanced microwave attenuation in titanate perovskites. *Adv Mater*. 2023;35(11):2210243. <https://doi.org/10.1002/adma.202210243>.
- [42] Du YQ, Yan ZK, You WB, Men QQ, Chen GY, Lv XW, Wu YY, Luo K, Zhao B, Zhang JC, Che RC. Balancing MXene surface termination and interlayer spacing enables superior microwave absorption. *Adv Funct Mater*. 2023;33(34):2301449. <https://doi.org/10.1002/adfm.202301449>.
- [43] Wen CY, Li X, Zhang RX, Xu CY, You W, Liu ZW, Zhao B, Che RC. High-density anisotropy magnetism enhanced microwave absorption performance in Ti<sub>3</sub>C<sub>2</sub>T<sub>x</sub> MXene@Ni microspheres. *ACS Nano*. 2022;16(1):1150. <https://doi.org/10.1021/acsnano.1c08957>.
- [44] Wu XM, Xie F, Yao YL, Sun Y, Hua ZS, Zhao Z, Yang YX. Template-free preparation of porous Co microfibers from spent lithium-ion batteries as a promising microwave absorber. *Rare Met*. 2022;41(10):3475. <https://doi.org/10.1007/s12598-022-02034-w>.
- [45] Wang HC, Xiang L, Wei W, An J, He J, Gong CH, Hou YL. Efficient and lightweight electromagnetic wave absorber derived from metal organic framework-encapsulated cobalt nanoparticles. *ACS Appl Mater Interfaces*. 2017;9(48):42102. <https://doi.org/10.1021/acsami.7b13796>.
- [46] Zhao YH, Zhou Z, Chen GX, Li QF. Coaxial double-layer-coated multiwalled carbon nanotubes toward microwave absorption. *Mater Lett*. 2018;233:203. <https://doi.org/10.1016/j.matlet.2018.09.010>.
- [47] Liu Y, Zeng ZH, Zheng SN, Qiao J, Liu W, Wu LL, Liu JR. Facile manufacturing of Ni/MnO nanoparticle embedded carbon nanocomposite fibers for electromagnetic wave absorption. *Compos Part B Eng*. 2022;235:109800. <https://doi.org/10.1016/j.compositesb.2022.109800>.
- [48] Liang LY, Li QM, Yan X, Feng Y, Wang Y, Zhang HB, Zhou XP, Liu CT, Shen CY, Xie XL. Multifunctional magnetic Ti<sub>3</sub>C<sub>2</sub>T<sub>x</sub> MXene/graphene aerogel with superior electromagnetic wave absorption performance. *ACS Nano*. 2021;15(4):622. <https://doi.org/10.1021/acsnano.0c09982>.
- [49] Gao ZG, Yang K, Zhao ZH, Lan D, Zhou Q, Zhang JQ, Wu HJ. Design principles in MOF-derived electromagnetic wave absorption materials: review and perspective. *Int J Miner Metall Mater*. 2023;30(3):405. <https://doi.org/10.1007/s12613-022-2555-8>.
- [50] Gao J, Ma ZJ, Liu FL, Weng XY. Synthesis and electromagnetic wave absorption properties of Gd-Co ferrite@carbon core-shell structure composites. *Rare Met*. 2022. <https://doi.org/10.1007/s12598-022-02123-w>.
- [51] Yuan MY, Lv HL, Cheng HW, Zhao B, Chen GY, Zhang JC, Che RC. Atomic and electronic reconstruction in defective 0D molybdenum carbide heterostructure for regulating lower-frequency microwaves. *Adv Funct Mater*. 2023;33(33):2302003. <https://doi.org/10.1002/adfm.202302003>.
- [52] Xing Y, Fan YC, Yan ZK, Zhao B, Huang YJ, Pan W. Core-shell LaOCl/LaFeO<sub>3</sub> nanofibers with matched impedance for high-efficiency electromagnetic wave absorption. *Sci China-Mater*. 2023;66(4):1587. <https://doi.org/10.1007/s40843-022-2264-9>.
- [53] Yu D, Shi GM, Shi FN, Bao XK, Li ST, Li Q. N-doped carbon nanofiber embedded with TiN nanoparticles: a type of efficient microwave absorbers with lightweight and wide-bandwidth. *J Alloys Compd*. 2022;920:165791. <https://doi.org/10.1016/j.jallcom.2022.165791>.
- [54] Deng WB, Li TH, Li H, Niu RP, Dang AL, Cheng YL, Wu HJ. In situ construction of hierarchical core-shell SiCnws@SiO<sub>2</sub>-carbon foam hybrid composites with enhanced polarization loss for highly efficient electromagnetic wave absorption. *Carbon*. 2023;202:103. <https://doi.org/10.1016/j.carbon.2022.10.081>.
- [55] Zhao B, Du Y, Lv H, Yan Z, Jian H, Chen G, Wu Y, Fan B, Zhang J, Wu L, Zhang DW, Che R. Liquid-metal-assisted programmed galvanic engineering of core-shell nanohybrids for microwave absorption. *Adv Funct Mater*. 2023;33(34):2302172. <https://doi.org/10.1002/adfm.202302172>.
- [56] Wang P, Liu PA, Ye S. Preparation and microwave absorption properties of Ni(Co/Zn/Cu)Fe<sub>2</sub>O<sub>4</sub>/SiC@SiO<sub>2</sub> composites. *Rare Met*. 2019;38(1):59. <https://doi.org/10.1007/s12598-016-0752-1>.
- [57] Cui XQ, Liang XH, Liu W, Gu WH, Ji GB, Du YW. Stable microwave absorber derived from 1D customized heterogeneous structures of Fe<sub>3</sub>N@C. *Chem Eng J*. 2020;381:122589. <https://doi.org/10.1016/j.cej.2019.122589>.
- [58] Zheng XL, Feng J, Zong Y, Miao H, Hu XY, Bai JT, Li XH. Hydrophobic graphene nanosheets decorated by monodispersed superparamagnetic Fe<sub>3</sub>O<sub>4</sub> nanocrystals as synergistic electromagnetic wave absorbers. *J Mater Chem C*. 2015;3(17):4452. <https://doi.org/10.1039/C5TC00313J>.
- [59] Zhang ZD, Li ZH, Zhao YH, Bi XR, Zhang ZY, Long ZK, Liu ZX, Zhang LJ, Cai WJ, Liu Y, Fan RH. Dielectric enhancement effect in biomorphic porous carbon-based iron@iron carbide 'meta-powder' for light-weight microwave absorption material design. *Adv Compos Hybrid Mater*. 2022;5(4):3176. <https://doi.org/10.1007/s42114-022-00445-y>.
- [60] Guo SN, Zhang YQ, Chen JB, Wu Y, Cao JM, Tang SL, Ji GB. The excellent electromagnetic wave absorbing properties of carbon fiber composites: the effect of metal content. *Inorg Chem Front*. 2022;9(13):3244. <https://doi.org/10.1039/D2QI00854H>.
- [61] Shen YQ, Zhang F, Song PF, Zhang YC, Zhang T, Wen XQ, Ma JQ, Zhang D, Du XY. Design and synthesis of magnetic porous carbon nanofibers with excellent microwave absorption. *J Alloys Compd*. 2022;903:163971. <https://doi.org/10.1016/j.jallcom.2022.163971>.
- [62] Zhang ZY, Zhao YH, Li ZH, Zhang LJ, Liu ZX, Long ZK, Li YJ, Liu Y, Fan RH, Sun K, Zhang ZD. Synthesis of carbon/SiO<sub>2</sub> core-sheath nanofibers with Co-Fe nanoparticles embedded in via electrospinning for high-performance microwave absorption. *Adv Compos Hybrid Mater*. 2022;5(1):513. <https://doi.org/10.1007/s42114-021-00350-w>.
- [63] Lv J, Liang XH, Ji GB, Quan B, Liu W, Du YW. Structural and carbonized design of 1D FeNi/C nanofibers with conductive network to optimize electromagnetic parameters and absorption abilities. *ACS Sustain Chem Eng*. 2018;6(6):7239. <https://doi.org/10.1021/acssuschemeng.7b03807>.
- [64] Dong SX, Li J, Zhang S, Li N, Li B, Zhang QL, Ge LQ. Excellent microwave absorption of lightweight PAN-based

- carbon nanofibers prepared by electrospinning. *Colloids Surf-Physicochem Eng Asp.* 2022;651: 129670. <https://doi.org/10.1016/j.colsurfa.2022.129670>.
- [65] Li Y, Liu XF, Nie XY, Yang W, Wang YD, Yu RH, Shui JL. Multifunctional organic–inorganic hybrid aerogel for self-cleaning, heat-insulating, and highly efficient microwave absorbing material. *Adv Funct Mater.* 2019;29(10):1807624. <https://doi.org/10.1002/adfm.201807624>.
- [66] Chen JB, Zheng J, Wang F, Huang QQ, Ji GB. Carbon fibers embedded with FeIII-MOF-5-derived composites for enhanced microwave absorption. *Carbon.* 2021;174:509. <https://doi.org/10.1016/j.carbon.2020.12.077>.
- [67] Zhao B, Du YQ, Yan ZK, Rao LJ, Chen GY, Yuan MY, Yang LT, Zhang JC, Che RC. Structural defects in phase-regulated high-entropy oxides toward superior microwave absorption properties. *Adv Funct Mater.* 2023;33(1):2209924. <https://doi.org/10.1002/adfm.202209924>.
- [68] Zhao ZH, Zhang LM, Wu HJ. Hydro/organo/ionogels: “controllable” electromagnetic wave absorbers. *Adv Mater.* 2022; 34(43):2205376. <https://doi.org/10.1002/adma.202205376>.
- [69] Shen X, Yang SH, Yin PG, Li CQ, Ye JR, Wang GS. Enhancement in microwave absorption properties by adjusting the sintering conditions and carbon shell thickness of Ni@C submicrospheres. *CrystEngComm.* 2022;24(4):765. <https://doi.org/10.1039/D1CE01525G>.
- [70] Huang LX, Duan YP, Pang HF. Thin layers of microwave absorbing metamaterials with carbon fibers and FeSi alloy ribbons to enhance the absorption properties. *EPJ Appl Metamater.* 2023;10:3. <https://doi.org/10.1051/epjam/2022019>.
- [71] Liang HS, Chen G, Liu D, Li ZJ, Hui S, Yun JJ, Zhang LM, Wu HJ. Exploring the Ni 3d orbital unpaired electrons induced polarization loss based on Ni single-atoms model absorber. *Adv Funct Mater.* 2023;33(7):2212604. <https://doi.org/10.1002/adfm.202212604>.

Springer Nature or its licensor (e.g. a society or other partner) holds exclusive rights to this article under a publishing agreement with the author(s) or other rightsholder(s); author self-archiving of the accepted manuscript version of this article is solely governed by the terms of such publishing agreement and applicable law.